Automatic detection of industrial wire rope surface damage using deep learning-based visual perception technology

Ping Zhou, Gongbo Zhou, *Senior Member, IEEE*, Houlian Wang, Dongxu Wang and Zhenzhi He

***Abstract*—Surface wear, which is most likely to occur in early damage of wire ropes (WRs), is a serious threat to WR safety. Visual perception technology (VPT) can intuitively grasp the surface damage situation of WRs. However, efficient detection of WR surface damage from complex morphological characteristics using VPT has always been a challenging task, and there are various problems, such as non-standard data, low automation/intelligence, and poor detection effect. To overcome the above difficulties, this study proposes a deep learning-based VPT framework, which relies on an image preprocessing (IP) scheme and a deep convolutional neural network (DCNN), called WR-IPDCNN. The IP scheme is designed to remove the influence of the image background and to normalize data, including posture adjustment and region of interest (ROI) extraction. The improved DCNN based on LeNet-5 is proposed to mine the newly established WR dataset, which considers different working conditions. Experimental results demonstrate that the proposed framework can accurately extract the ROI area of WR images and achieve 95.55% detection accuracy, which is 12.44% higher than LeNet-5, and a significant improvement on the automation/intelligence level in this field.**

***Index Terms*—Visual perception, Surface damage, Intelligent detection, Deep convolutional neural network, Wire rope.**

I. INTRODUCTION

As the key load-bearing component, wire ropes (WRs) are the core of complex industrial rope systems, such as mine hoists, engineering cranes, ropeways, building elevators, etc. [1-3]. Once an accident occurs caused by the WR in the lifting or towing process, it will lead to serious life/property losses and terrible social impacts [4]. For example, on December 29, 2004, 53 tourists were trapped as a result of the WRs breaking on a ropeway in Switzerland; on September 25, 2012, in a coal mine in Gansu province, China, an accident occurred in which the WRs broke, resulting in 20 deaths and 14 injuries; on November 7, 2018, the WRs of a tower crane broke at a construction site in Guangxi province, China, and a worker was killed after being hit by the hook.

Detection of early damage is a promising way to avoid WR accidents. The early damage mainly occurs on the surface because of the working characteristics of WRs (rubbing, twisting, or scratching repeatedly in exposed conditions), and the main damage is wear. With the deterioration of early wear, it will get worse and lead to the occurrence of broken wires, broken strands, and even broken ropes, which have a serious influence on the remaining life of WRs [5]. Thus, it is highly valuable and meaningful to investigate novel detection methods for WR early surface wear damage.

To detect and grasp the surface condition of WRs, the visual method is the most intuitive method compared with other detection methods [6]. This method can directly obtain the morphology characteristics of the damage without a complicated signal conversion process. Moreover, details of surface damage still require further visual inspection if non-visual methods are used. At present, the traditional visual method (artificial vision with touching) is mainly used for WR surface damage inspection in practice. However, traditional visual method has some shortcomings, including low efficiency, the miss-detection rate, and interference from human factors [7]. Therefore, given the rapid, efficient, and objective characteristics of visual perception technology (VPT), the development of VPT-based WR surface damage detection method is a vital way to replace artificial inspection or assist other detection methods to comprehensively characterize the state of WRs.

Detecting the surface damage of industrial objects through VPT has drawn a lot of attention [8-11]; this is also the case in the field of WR surface damage detection. Alberto *et al*. [12] designed a measurement system based on the mathematical model of the rope contour to detect the damage by measuring the change in rope length. To detect WR surface defects, Platzer *et al*. [13] studied the influence of different texture features on detection performance. They proposed a hidden Markov model-based method to detect and locate defects [14]. A detection method based on support vector data description (SVDD) was proposed for control-WR in aircraft by Sun *et al*. [15]. To realize the detection of abnormal surfaces of WRs, Wacker et al. [16] established a probabilistic model combining the structure and appearance of WRs. Orhan *et al*. [17]

Manuscript received March 16, 2020. This work was supported by the National Key Research and Development Program (2016YFC0600905), by the Jiangsu Provincial Outstanding Youth Fund of China (BK20180033), and by the Project Funded by the Priority Academic Program Development of Jiangsu Higher Education Institutions (PAPD). (*Corresponding author: Gongbo Zhou*).

P. Zhou, G. Zhou, and D. Wang are with Jiangsu Key Laboratory of Mine Mechanical and Electrical Equipment, School of Mechatronic Engineering, China University of Mining and Technology, Xuzhou 221116, Jiangsu Province, China. (e-mail: gbzhou@cumt.edu.cn).

H. Wang is with School of Mechanical and Electrical Engineering, Jiangsu University of Science and Technology, Zhenjiang 212000, Jiangsu Province, China.

Z. He is with School of Mechanical and Electrical Engineering, Jiangsu Normal University, Xuzhou 221116, Jiangsu Province, China.

proposed a method using image processing and autocorrelation to monitor elevator rope faults. Zhou *et al*. [18] proposed a texture-based WR defect detection approach, and compared the diagnostic effect of different machine learning (ML) algorithms.

The above examples [12-18] provide some meaningful methods for WR surface damage detection. However, there are some problems that need to be further addressed:

1) *Non-standard data*. As a result of the influence of the WR shaking, the obtained WR image is not always located in the middle of the image in horizontal or vertical posture; the acquired image contains a large amount of background information, thereby causing unnecessary calculations and affecting the diagnosis result.
2) *Low detection automation/intelligence*. There is a lack of automatic methods for obtaining standard data; the existing diagnostic methods need to select and extract features manually, because ML cannot generate discriminative features from the original data.
3) *Poor detection effect*. There is still a lack of reliable and high-precision damage detection methods for WRs, especially for early surface wear. This is caused by insufficient reasonable image preprocessing methods and limited performance of traditional ML algorithms.

With the rapid development of ML, deep learning (DL) [19] is considered as an efficient way to solve the above problems combined with appropriate image preprocessing (IP) method. As one of the most efficient DL methods, convolutional neural network (CNN) simulates the mechanism of human visual perception and uses multiple cortex layers to recognize the structural information of perceptual objects, and can therefore adaptively learn the deep expression of features from the original data and avoid the complicated artificial feature extraction process [20, 21]. On this basis, these methods have been greatly developed in the field of image-based damage detection or fault diagnosis [22-26].

Therefore, a novel DL-based surface damage detection method for WRs is proposed in this paper, based on the ability/potential of CNN in adaptive features extraction and diagnostic performance, and the function of appropriate preprocessing methods in improving the accuracy and efficiency of the results [27]. First, a new WR IP method is provided to remove the background information and normalize irregular WR image data. Then, a new improved CNN is put forward to adaptively extract the surface damage features of the WR. At the same time, a circumferential vision perception system of the WR surface image is proposed, a WR dataset is established, some experiments and comparative studies are carried out, and finally, the feasibility of the proposed architecture is demonstrated and the best results are obtained.

To our best knowledge, this is a pioneering work, and there are no relevant studies focused on surface damage detection of WRs using DL methods. Meanwhile, the results demonstrate that it is a great advance in the monitoring and diagnosis of WR surface damage. The main contributions of this paper are summarized in the following three points:

1) To standardize the irregular WR surface image data, a new WR image preprocessing scheme is proposed to overcome WR shaking and remove unnecessary background information from the WR image;
2) DL is introduced into the field of WR surface damage detection for the first time. An improved deep convolutional neural network (DCNN) based on LeNet-5 is proposed, using a deeper structure to adaptively extract features;
3) The proposed method obtains a higher accuracy than other traditional methods based on a new WR surface damage dataset, which considers different practical working situations.

This paper is organized as follows. Section II gives the framework of the proposed damage detection method. The detection modules including posture adjustment (PA), region-of-interest (ROI) extraction, and diagnosis and recognition method are described in Section III, respectively. The experiments and results are analyzed and summarized in detail in Section IV. In Section V, we compare and discuss our results with those of the published VPT-based works and other detection methods. Section VI presents the conclusions.

II. Proposed Method Framework

In practice, the dirt on the WR surface may affect damage detection. But it can be seen from Fig.1 that the surface texture of the WR is clear, and only a small amount of oil stain exists on the strands. The surface damage is the damage to the texture; so being able to detect the surface damage from the clear texture of the WR through the VPT is expected. In addition, with the development of WR surface cleaning devices, the visual inspection of WRs is affected to a lesser and lesser degree by oil pollution.

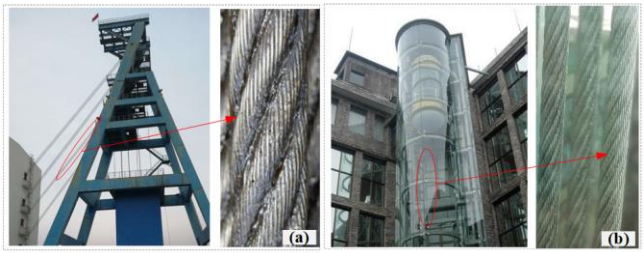

Fig. 1. Pictures of steel WRs (a)mine hoist (b) elevator

This section presents an overview of the proposed damage detection framework, which is composed of several parts and is called WR-IPDCNN. Specifically, the framework of this method is illustrated in Fig. 2. The detailed processes are as follows:

Step1*: Image acquisition.* Real-time circumferential acquisition of the WR image in the actual operation of the system, which records the position of each image of the whole rope, so as to provide positional parameters for early warning.

Step2: *Original image preprocessing.*

Step 2.1: Position adjustment. Filtering, texture detection, and morphological methods are used to realize the WR image segmentation; then the Hough transform is used to realize the boundary recognition. The boundary slope is calculated, and then the image is rotated.

This article has been accepted for publication in a future issue of this journal, but has not been fully edited. Content may change prior to final publication. Citation information: DOI 10.1109/TIM.2020.3011762, IEEE Transactions on Instrumentation and Measurement

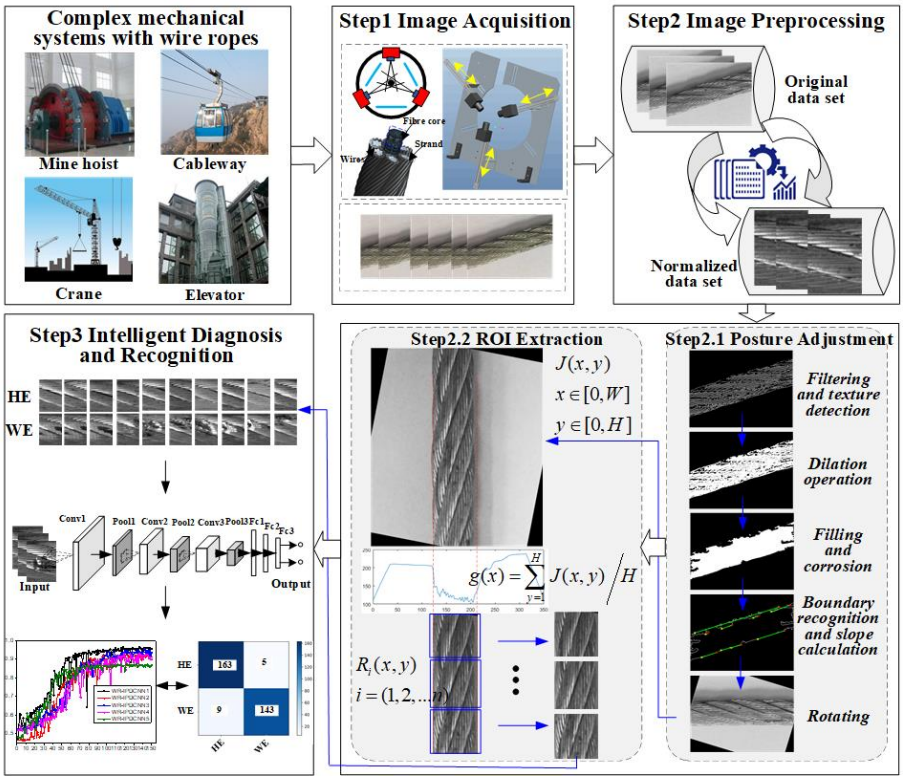

Fig. 2. Framework of the WR-IPDCNN method. Step1: image acquisition, Step2: image preprocessing, Step3: intelligent diagnosis and recognition.

Step 2.2: ROI extraction. A vertical grayscale projection map is achieved from the vertical grayscale projection of the image. According to the diameter of the WR and gray integral formula, the interval with the smallest gray integral value is calculated and cut out, and then divided into sub-graphs of equal length.

Step3*: WR-IPDCNN classifier development*. The normalized image is divided into a training set and test set. The structure and parameters of the WR-IPDCNN are set, and the WR-IPDCNN is trained and tested to obtain a deep network model that meets the requirements of accuracy and efficiency.

III. DAMAGE DETECTION MODULES

A proper preprocessing method is helpful to eliminate environmental and background effects, reduce computational effort, normalize data, and improve the final detection outcome. This section explains the proposed method in detail, that is, the posture adjustment is first performed, then the ROI area is extracted, and finally, the WR-IPDCNN model is established.

A. Posture adjustment

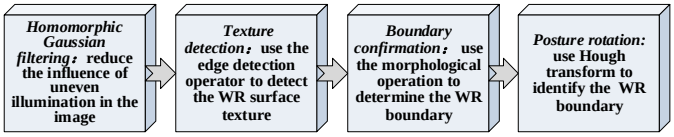

Fig. 3. Block diagram of the posture adjustment.

Due to the existence of texture, the WR surface exhibits large changes in gray level, and the morphological operation can be performed on the basis of the texture identification. This helps realizing the segmentation and boundary recognition of the WR image. On this basis, posture adjustment can be realized. We designed a general pipeline to adjust the position of different sizes of WRs, as shown in Fig. 3. Details are as follows:

1) Homomorphic Gaussian filtering. First, the original image is filtered by a homomorphic Gaussian filtering algorithm to make the illumination uniform, enhance the details of the dark areas in the image, and reduce the influence of image shadows [28]. We designed a homomorphic Gaussian low-pass filter:

$$H_{hf}(u,v)=(\gamma_H-\gamma_L)\left[cH_l(u,v)\right]+\gamma_L \tag{1}$$

In the formula:

$$H_l(u,v)=\exp\left[-(D(u,v)/D_0)^{2n}\right] \tag{2}$$

where $H_{hf}(u,v)$ is the homomorphic filter, $H_l(u,v)$ is the low-pass filter, D_0 represents the cut-off frequency, $D(u,v)=\sqrt{u^2+v^2}$, and n represents the order. c is a constant that is between γ_H and γ_L, and it can control the slope sharpness ($\gamma_L<1$, $\gamma_H>1$).

2) Texture detection. Then, the edge detection operator is used to detect the WR texture to obtain a binary image, in preparation for the morphological operation. The Sobel operator [29] is used to detect the WR texture. It judges whether the gray value of this point reaches the threshold to detect the edge. For an image $f(x, y)$, the gradient image $G(x, y)$ can be defined as:

$$G(x,y)=\sqrt{G_x^{\,2}(x,y)+G_y^{\,2}(x,y)} \tag{3}$$

where (x, y) is the location of each pixel. In the formula:

This article has been accepted for publication in a future issue of this journal, but has not been fully edited. Content may change prior to final publication. Citation information: DOI 10.1109/TIM.2020.3011762, IEEE Transactions on Instrumentation and Measurement

$$G_x(x,y)=\sum_{i=-1}^{1}\sum_{j=-1}^{1} f(x+i,y+j)a_x(i,j) \tag{4}$$

$$G_y(x,y)=\sum_{i=-1}^{1}\sum_{j=-1}^{1} f(x+i,y+j)a_y(i,j) \tag{5}$$

where $a_x(i,j)$ and $a_y(i,j)$ are the Sobel edge operators in the *x*-axis and *y*-axis, respectively; if the gray value of point (*x*, *y*) is greater than a certain threshold in the gradient image *G*(*x*, *y*), the point (*x*, *y*) is identified as an edge point. Then, the gradient direction is obtained:

$$\theta=\arctan(\frac{G_y(x,y)}{G_x(x,y)}) \tag{6}$$

3) Boundary confirmation. Next, the morphological operation [30] is used to determine the WR boundary. The texture binary image is dilated by the dilation morphology algorithm, the holes are filled, and then the image is subjected to twice smooth erosion. For binary image *A*, if *B* is a structural element, then *A* is dilated by *B* and can be defined as:

$$A\oplus B=\left\{z\left|\left[(\hat{B})_z\cap A\right]\neq\varnothing\right.\right\} \tag{7}$$

A is corroded by *B* and can be defined as:

$$A\odot B=\left\{z\left|(B)_z\subseteq A\right.\right\} \tag{8}$$

The dilation operation can enlarge the texture of the WR, the hole filling can fill the gap, and the twice smooth erosion process can reduce the increasing edge of the WR due to the dilation process, and consequently, the WR boundary is more accurate. Through the above process, the WR can be segmented from the image background and the boundary is determined to prepare it for the posture adjustment.

4) Posture rotation. Finally, the boundary of the WR segmentation map is identified using the Hough transform method [31], and the slope of the boundary is calculated. Then, the WR is rotated to a specified angle. The Hough transform method fits the line and curve by transforming the image coordinate space into the parameter space. The straight line, expressed in the Cartesian coordinate parameter space and the polar coordinate parameter space, can be formulated as:

$$\begin{cases} y=ax+b \\ \rho=x\cos\theta+y\sin\theta \end{cases} \tag{9}$$

where *a* is the slope, *b* represents the intercept, ρ is the distance from the straight line to the origin, and θ denotes the angle from the *x*-axis to the straight line, whose value ranges from minus 90 degrees to plus 90 degrees. Taking a Cartesian coordinate system as an example, there are an infinite number of straight lines passing through the points, corresponding to different *a* and *b* values. This is similar for the point (x_j,y_j). The following transformation is obtained:

$$\begin{cases} b=-x_i a+y_i \\ b=-x_j a+y_j \end{cases} \tag{10}$$

Each point on the straight line of the point (x_i,y_i) and (x_j,y_j) in the image coordinate space corresponds to a straight line in the parameter space. These lines intersect at the point (a_0,b_0), which is the line parameter determined by point (x_i,y_i) and (x_j,y_j) in the image coordinate space. According to this characteristic, given some edge points of the image coordinate space, the line equation connecting these points can be determined by the Hough transform method.

In conclusion, this method can separate the foreground WR from the background in the image and adjust its angle. The various steps of the proposed WR posture hybrid adjustment method are summarized in **Algorithm 1**, named WR-PA.

Algorithm 1. WR-PA: WR posture adjustment algorithm

Input: Unadjusted WR initial image I

Output: Adjusted WR image J

1: Homomorphic Gaussian filtering
Set the parameters in Equation (1) and (2), r_H, r_L, *c*, *n*, D_0. Filter the image I to obtain a filtered image I1.

2: Texture detection
Set the threshold *g* of the Sobel. Calculate the gradient image *G*(*x*, *y*) according to Equation (3), and compare it with the threshold. If the gray value greater than the threshold, then the binary texture image I2 is obtained.

3: Boundary confirmation
3.1: Set the structural element *B*1, and the dilation operation is performed to obtain the expanded image I3;
3.2: Perform the hole filling operation to obtain the filled image I4;
3.3: Set the structural element *B*2, and the erosion operation is performed twice to obtain the corroded image I5.

4: Attitude rotation
4.1: Perform the Hough transform, set the number of peaks to seek the peak value, and extract the straight line segment (the merge threshold of line segment and the minimum length of the detected line segment are set), then the WR boundary line is found, and the WR boundary image I6 is obtained.
4.2: Calculate the slope of the boundary, then rotate the filtered image I1. After the rotation is completed, a rotated image J is obtained.

B. ROI extraction

To reduce the background influence and computational cost, and to further normalize the data, we propose a ROI extraction algorithm based on gray projection for WR images, named WR-ROI, after adjusting the WR posture. The valuable WR area picture *R*(*x*, *y*) is extracted, namely the ROI area, from the adjusted WR image *J*(*x*, *y*). The width of image *J*(*x*, *y*) is set as *W*, and the height is *H*. For the input image *J*(*x*, *y*), we can calculate the average gray value of the *x*th column:

$$g(x)=\sum_{y=1}^{H} J(x,y)/H \tag{11}$$

Then the projection of the image *J* in the vertical direction is $G=[g(1),g(2),...g(W)]$ [32]. The width of the WR is set to *W*r, and the grayscale integral *S*(*d*) of each width in the projection curve along the x-axis is:

$$S(d)=\sum_{k=1}^{Wr} g(d+k),\ 1\le d\le W-Wr \tag{12}$$

When *d* satisfies $\arg\min S(d)$, we can get that *d* is the starting position of the WR in the *x*-axis direction, and *d*+*W*r is the end position (the maximum or the minimum value of *S*(*d*) is set according to the relative gray level between the WR and the background). Then, the map in the interval [*d*, *d*+*W*r] in the *x*-axis direction is the ROI region *R*(*x*, *y*) (it can add a certain width on both sides of ROI as required). After *R*(*x*, *y*) is cut and divided into sub-graphs of equal length, the dataset is formed. It

This article has been accepted for publication in a future issue of this journal, but has not been fully edited. Content may change prior to final publication. Citation information: DOI 10.1109/TIM.2020.3011762, IEEE Transactions on Instrumentation and Measurement

is summarized in **Algorithm 2**.

Algorithm 2. WR-ROI: WR region-of-interest extraction algorithm

Input: Adjusted WR image J

Output: ROI image K

1: Rotate the WR in the image to the vertical form.

2: Perform grayscale vertical projection according to Equation (11).

3: Set the image width Wr, calculate the grayscale integral $S(d)$ in the x-axis direction using Equation (12), and when $\arg\min S(d)$ is satisfied, the WR interval $[d, d+Wr]$ is obtained.

4: Cut the WR region according to the interval $[d, d+Wr]$, then set the sub-image length L and divide it to get the ROI image K (the size is $L \times Wr$). Return to step1.

C. Diagnosis and recognition

LeNet-5 is a classic CNN structure [24], and many other structures have generally been improved and optimized according to it. There are two alternating convolutional and pooling layers in this model, with a two-layer fully connected artificial neural network, which has been widely applied in the mechanical diagnosis field [21-25] to provide powerful approaches for damage/fault diagnosis and recognition tasks. It is a tool that can be adapted to specific tasks to enhance the relevant performance [33].

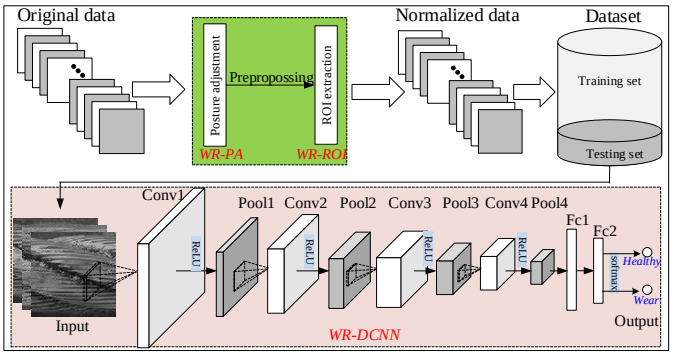

Fig. 4. Proposed WR-IPDCNN architecture.

TABLE I. THE CONFIGURATIONS OF THE CONVOLUTION (CONV), POOLING (POOL), AND FULLY CONNECTED (FC) LAYERS.

Layer	Parameters information	Variables	Output data dimension
Conv1	16 convolution kernels with 5×5, stride is 1	416	16×96×96
Pool1	MaxPooling size 2×2, stride is 2	0	16×48×48
Conv2	32 convolution kernels with 3×3, stride is 1	4640	32×48×48
Pool2	MaxPooling size 2×2, stride is 2	0	32×24×24
Conv3	64 convolution kernels with 3×3, stride is 1	18496	64×24×24
Pool3	MaxPooling size 2×2, stride is 2	0	64×12×12
Dropout	0.2	0	64×12×12
Conv4	96 convolution kernels with 3×3, stride is 1	55392	96×12×12
Pool4	Pooling size 2×2, stride is 2	0	96×6×6
Dropout	0.2	0	96×6×6
FC1	120 nodes	414840	1×120
FC2	32 nodes	3872	1×32
Output	2 nodes	66	1×2

In this study, the CNN model based on LeNet-5 is designed to solve the WR damage monitoring and diagnosis task. Combined with the preprocessing steps above, we propose the WR-IPDCNN structure. The basic structure of the proposed WR-IPDCNN model with a preprocessing section, which contains four alternating intermediate layers of CNN, is shown in Fig. 4. The configurations of the proposed WR-IPDCNN are listed in Table I.

IV. EXPERIMENTS AND RESULTS

In this section, to evaluate the proposed WR-IPDCNN method: a feasible scheme for the image visual perception system is firstly introduced, experiments are carried out, and finally, the results are analyzed and discussed clearly.

A. Visual perception system

A feasible visual perception system scheme for image acquisition and processing is presented in Fig.5.

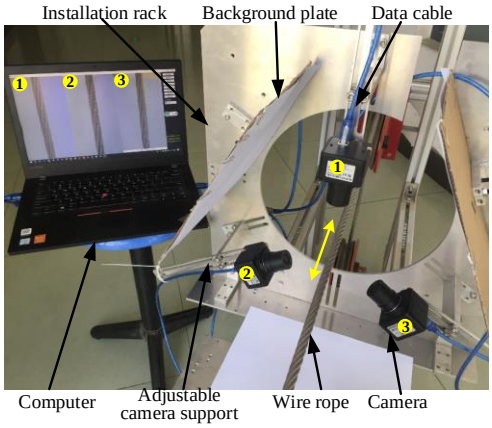

Fig. 5. A feasible visual perception scheme for image acquisition and processing.

The main components of the system are the camera, the installation rack, the adjustable camera support, the background plate, the computer, the data cable, etc. The adjustable camera support can adjust the distance between the camera and the WR. The color selection of the background plate should have a gray difference as compared with the WR (here, we choose pure white). Three 120-degree cameras collect the WR surface image in the circumferential direction, and each one does not interfere with the other in the imaging process. The computer specifications are as follows: Intel Core i5-6200U 2.40 GHz CPU with 8.00 GB memory (hardware environment), and Windows 10 of 64 bits (software environment). Offline acquisition and processing of images is completed using the computer. The data is preprocessed using the proposed IP scheme, and the data are mined using the proposed improved DCNN in Keras.

B. Experiments and comparison with other learning algorithms

1) Dataset Establishment. According to the analysis in the Section II, the texture of the WR is, in practice, generally clear, and the surface damage of the WR is the damage to the texture. So we need to build WR dataset with various samples of wear damage on clear surface textures. In general, the WRs on site are healthy, and it is difficult to collect a complete and abundant qualified data including health and wear states from the field. Therefore, according to the general process of dataset

establishment in the deep learning task [34-36], we made a simulation dataset based mainly on laboratory data combined with the actual situation. We first collected the WR pictures of a shallow well on site, and then collected the pictures in the laboratory. In order to improve the robustness and adaptability of the algorithm, we fine-tuned the illumination, size, and lubrication conditions on the basis of ensuring clear texture in the data acquisition process in laboratory, that is, the collected data came from varying natural lighting conditions, sizes (WR diameter 18 cm/10 cm; picture size 140×140 pixels/100×140 pixels), and relative lubrication conditions (clean/ oily).

In the laboratory, before image acquisition, we first produced wear damage, and then oiled part of the WRs (simulating the oil stains of WRs in shallow well). In the process of wear manufacturing, a grinding wheel was used by different people to cause damage of different depths, lengths, widths, and wear angles, at random. Then, some WRs were coated with oil stains. After that, healthy and worn WR images were continuously collected offline under natural light, and the ROI area was uniformly intercepted by the preprocessing algorithm. Finally, enough samples were selected to make up the dataset. Therefore, the dataset was established through grinding, oiling, image acquisition, posture adjustment, ROI extraction and selection. Through the aforementioned process, the obtained data are close to the actual situations.

In the posture adjustment process, the parameters in **Algorithm 1** need to be determined according to the testing effect. For this task, after a series of testing experiments, the parameters are set as follows:

- In homomorphic Gaussian filtering, γ_H=2.2, γ_L=0.25 , c=2, n=1, D_0=50 ;
- In texture detection, g=0.5g' (g' is the adaptive threshold);
- In boundary confirmation, there are two variables: Dilation: the linear structural element has an element length of 3 and an angle of 0 and 90 degrees; Erosion: a diamond-shaped structural element with a distance of 1 from the origin of the structural element to the vertex;
- In attitude rotation, the number of peaks is set to 4, and the first 4 peaks larger than 0.3 times the maximum value in the Hough matrix are found. The merge threshold of line segment is set to 50, and the minimum length of the detected straight line segment is set to 70.

The posture adjustment processes are depicted in Fig. 6. Several tests show that the algorithm is robust to illumination, WR size, and WR posture and background.

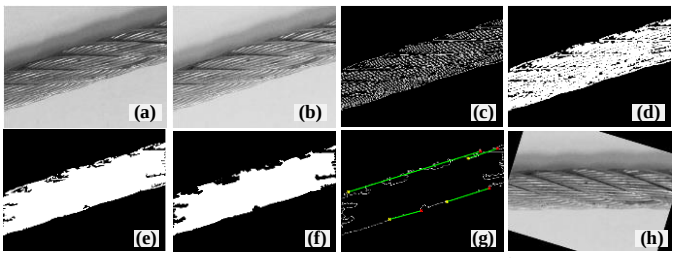

Fig. 6. Posture adjustment process. (a) original image I, (b) filtered image I1, (c) binary texture image I2, (d) dilation operation image I3, (e) filling operation image I4, (f) erosion operation image I5, (g) boundary image I6, (h) rotated image J.

Then, the **Algorithm 2** is used to extract the WR ROI. We select several samples as shown in Fig.7, including clean/oily samples with different sizes and different illumination conditions.

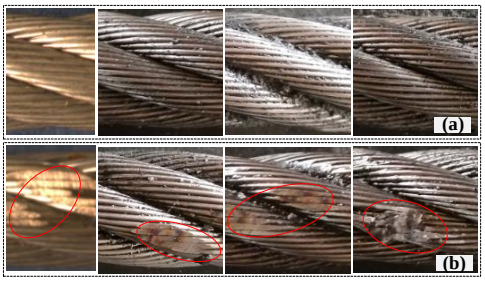

Fig. 7. Sample pictures. (a) healthy (b) wear.

Finally, 820 different healthy (HE) WRs and 780 different worn (WE) WRs are collected, the data set is named Image-data. Although the sample size is not very large, it is enough to train a robust classifier. In fact, in the process of using a CNN for surface damage detection, the number of samples required for different tasks is not certain, and the sample size of a single category varies from dozens [37] and hundreds [34,38-40], to thousands and above [35-36,41] (in this case, data enhancement is generally used, but some prior knowledge will be inevitably introduced). Theoretically, the larger the sample size, the better the coverage of the feature space; but more computing resources are required. In practice, as a result of the varying difficulties of collecting data from different tasks and the differences in defects, the sample sizes that meet the requirements are different. However, in these tasks, the same type of samples needs to cover all the sample spaces as much as possible, and the established dataset can train a model that meets the performance requirements. Therefore, in this task, we followed this principle: establishing a dataset that covers all sample spaces as much as possible, and this dataset can make the model obtained good performance.

Among all 1600 samples, the size of 1400 samples is 140 × 140 pixels, and the diameter of the WR is 18 cm; in addition, on the basis of the CNN's invariance to structural information, the size of the WR was fine-tuned, that is, 200 samples with a size of 100 × 140 pixels, and the WR diameter is 10 cm. The difference between these 200 samples and the other 1400 samples in terms of size scale is equivalent to the introduction of noise. In 1400 samples, including 720 healthy samples, 15% of them (108 samples) were taken from images of a shallow well hoisting wire rope, and the rest were obtained in the laboratory; all 680 wear samples are laboratory-simulated damage samples. To sum up, the final dataset includes 1600 samples, including 720 healthy samples (620 with a resolution of 140 × 140 pixels, including 220 with oil stains; 100 with a resolution of 100 × 140 pixels, no oil), 680 wear samples (580 with a resolution of 140 × 140 pixels, including 163 with oil stains; 100 with a resolution of 100 × 140 pixels, no oil).

Therefore, as a laboratory study, this work can serve as a

This article has been accepted for publication in a future issue of this journal, but has not been fully edited. Content may change prior to final publication. Citation information: DOI 10.1109/TIM.2020.3011762, IEEE Transactions on Instrumentation and Measurement

concept proof and can be further improved or extended to practical application [34].

2) Testing and Analysis. During the experiment, 80% of the randomly partitioned datasets were used as training sets and 20% as testing sets, running five times and taking the average value. The structure and parameter configurations of the proposed WR-IPDCNN will affect the network performance. The adjustment of hyper-parameters is a necessary task in network setup. After several adjustments, the learning rate was set as 0.01, and the batch size was taken as 20. The network structure and the empirically specified parameters of each layer in the WR-IPDCNN are presented in Table I. In the experimental process, random initialization parameters and stochastic gradient descent (SGD) were used to train the network.

TABLE II. DIFFERENT STRUCTURES OF WR-IPDCNN.

No.	Network structure
WR-IP DCNN1	Input[1×96×96]–16C[5×5]–16P[2×2]-32C[3×3]–32P[2×2]–64C[3×3]–64P[2×2]-96C[3×3]–96P[2×2]–FC[120–32]–Output[2]
WR-IP DCNN2	Input[1×96×96]–16C[5×5]–16P[2×2]-32C[3×3]–32P[2×2]–64C[3×3]–64P[2×2]-**120**C[3×3]–**120**P[2×2]–FC[120–32]–Output[2]
WR-IP DCNN3	Input[1×96×96]–16C[5×5]–16P[2×2]-32C[3×3]–32P[2×2]–64C[3×3]–64P[2×2]-96C[3×3]–96P[2×2]–FC[**64**–32]–Output[2]
WR-IP DCNN4	Input[1×96×96]–16C[5×5]–16P[2×2]-32C[3×3]–32P[2×2]–64C[3×3]–64P[2×2]-**120**C[3×3]–**120**P[2×2]–FC[**64**–32]–Output[2]
WR-IP DCNN5	Input[1×96×96]–16C[5×5]–16P[2×2]-32C[3×3]–32P[2×2]–64C[3×3]–64P[2×2]–FC[**64**–32]–Output[2]

Different network structures have a certain influence on diagnosis performance [24]. We fine-tuned the network structure, as shown in Table II. The results are shown in Fig.8.

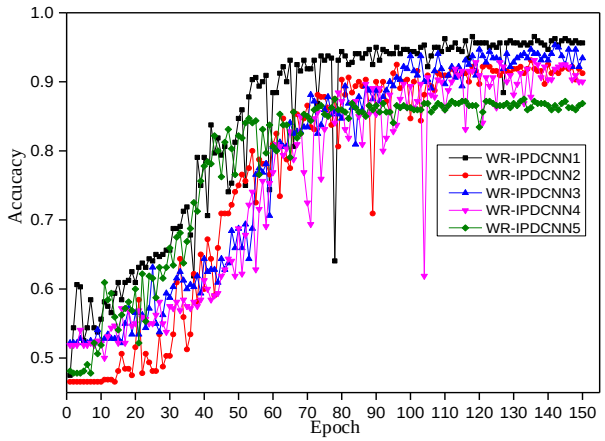

Fig. 8. Testing results of WR-IPDCNNs with 150 epochs.

The accuracy of WR-IPDCNN1-5 is 95.62%, 91.25%, 93.44%, 90%, and 86.87%, respectively. Fig.8 illustrates that the WR-IPDCNN1 obtained the best results, and WR-IPDCNN5 obtained the worst results because of the shallower structure. The other structures performed at various levels in between.

3) Comparison with Other Learning Algorithms. The proposed WR-IPDCNN is compared with a light architecture (namely, the classic LeNet-5) and two other traditional ML algorithms, namely, Support vector machine (SVM) and k-nearest neighbor (KNN), which are widely used in the field of pattern recognition. In the comparative experiments, the four algorithms were trained and tested using the same dataset: Image-data. The SVM and KNN were trained to obtain a better structure and configuration by fine-tuning. The output layer of LeNet-5 was changed to two nodes. The structure and configuration of WR-IPDCNN were selected with optimized performance through repeated experiments. The structure and configuration of each algorithm are presented in Table III.

TABLE III. THE STRUCTURE AND CONFIGURATION OF THE ALGORITHMS.

Algorithms	Structure and configuration
SVM	RBF kernel function, c = 50
KNN	k = 40, Euclidean distance
LeNet-5	Input [1×96×96]–6C[5×5]–6P[2×2]–16C[5×5]–16P[2×2]–FC[120–84]–Output[2]
WR-IPDCNN	Input[1×96×96]–16C[5×5]–16P[2×2]-32C[3×3]–32P[2×2]–64C[3×3]–64P[2×2]-96C[3×3]–96P[2×2]–FC[120–32]–Output[2]

The same training and testing method used in the previous section was applied here. The influence results of the parameters of SVM and KNN for the diagnosis accuracy are shown in Fig.9, and c = 50 and k = 40 were selected. The experimental results are depicted in Fig.10.

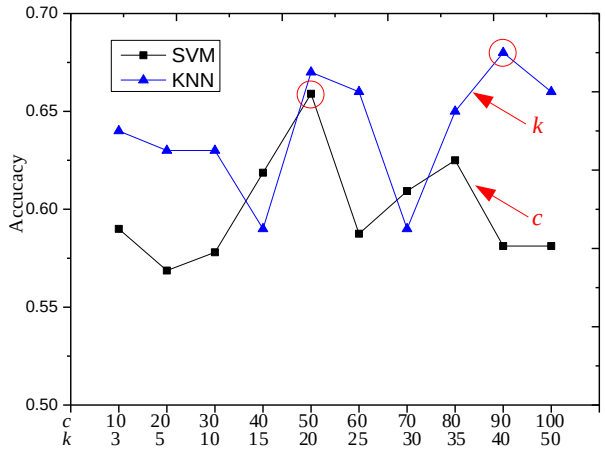

Fig. 9. The parameter influence of SVM and KNN.

Fig.10 shows that the accuracy of LeNet-5 and the proposed WR-IPDCNN is higher than that of SVM and KNN, demonstrating the advantages of DL in adaptive feature extraction. As a result of the lack of feature design and extraction, the performance of SVM and KNN is much lower than the expected value. As one of the most basic CNN structures, LeNet-5 has a much lower performance than WR-IPDCNN. It is illustrated that for a specific task, there is no specific CNN structure and configuration suitable for the task, and it is necessary to repeatedly adjust the parameters to obtain a better performance. In terms of time consumption, the average time consumption of SVM, KNN, LeNet-5, and WR-IPDCNN in each round of training was 84 s, 19 s, 7.5 s, 22.4 s, respectively, and the time consumption of WR-IPDCNN was between these values. For the DL method, as the depth increases, the time consumption also increases, but the time

This article has been accepted for publication in a future issue of this journal, but has not been fully edited. Content may change prior to final publication. Citation information: DOI 10.1109/TIM.2020.3011762, IEEE Transactions on Instrumentation and Measurement

cost of WR-IPDCNN is moderate (1 ms / sample), which can be accepted. Moreover, if a Graphic processing unit (GPU) is used, the time cost will be less.

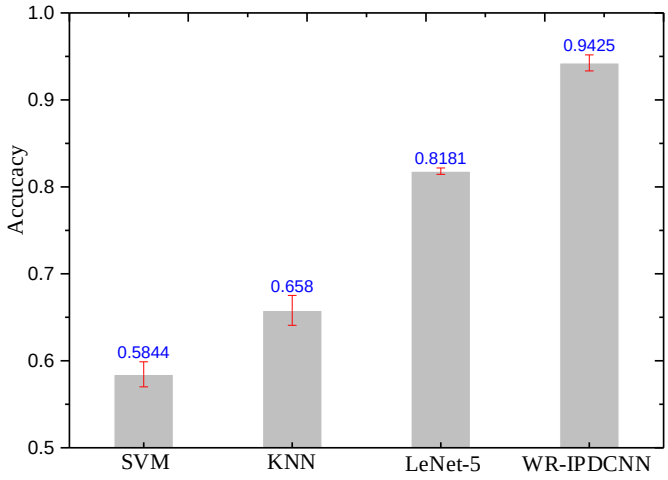

Fig. 10. Results comparison.

The confusion matrix is utilized to visualize the prediction results of each algorithm; we take one of the five experiments, as displayed in Fig.11. In addition, the prediction precision of each algorithm in each category is calculated and is listed in Table IV.

It can be seen from Fig.11 and Table IV that the DL method has similar recognition effects on the identification of each damage category, while the ML algorithm has a large difference in each category, especially the SVM. For the SVM, the difference in recognition accuracy is 0.4891 between HE and WE, demonstrating that the DL network has a better distinguishing ability on this task. In the DL method, LeNet-5 and WR-IPDCNN produced various misidentifications for each category. For example, LeNet-5 recognized 17 HEs as WEs, 40 WEs as HEs, and WR-IPDCNN recognized 5 HEs as WEs, and 9 WEs as HEs. The proposed WR-IPDCNN has a low false recognition rate, indicating that the proposed method has a higher precision in this task. At the same time, the results show that a slight degree of wear may be identified as a healthy state. Because a slight degree of wear has little effect on the health of steel WRs, this result is acceptable. The above conclusions further illustrate that the performance of DL in this task is better than ML, and the specific task requires a specific parameter configuration for a DL algorithm.

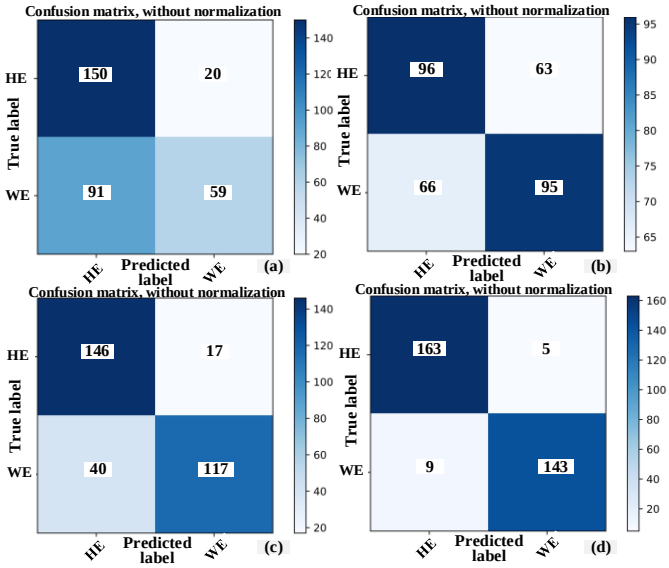

Fig. 11. Confusion matrix (a) SVM, (b) KNN, (c) LeNet-5, (d) Proposed WR-IPDCNN.

TABLE IV. THE PREDICTION PRECISION OF THE FOUR ALGORITHMS.

Algorithms	Healthy (HE)	Wear (WE)	Overall accuracy
SVM	0.8824	0.3933	0.6379
KNN	0.6038	0.5901	0.5970
LeNet-5	0.8957	0.7452	0.8204
WR-IPDCNN	0.9702	0.9408	**0.9555**

V. DISCUSSION AND ANALYSIS

In order to illustrate the advancement of this method and its promotion role of this field, we further compare and discuss this method with the published studies and other relevant non-destructive detection methods. It should be noted that it is not prudent to compare the detection accuracy of different methods under different settings, using different data, or in different working environment [42]. On this basis, we qualitatively analyze and compare each method.

1) Comparison and discussion with other visual methods. Among the VPT-based methods, there are model-based [12,16], signal-based [17], and data-driven methods [13-15,18]. The method in this paper is data-driven. Several representative studies are listed in Table V.

The model-based method relies on expert knowledge to build a complex mathematical model; the signal-based method relies on efficient signal processing and also needs sufficient expert knowledge; whilst the data-driven method only needs to feed

TABLE V. COMPARING WITH EXISTING REPRESENTATIVE WORKS

Representative methods	Types	Details	Accuracy
Re. [12]	Model-based	Mathematical model of rope contour + lay length detection	—
Re. [17]	Signal-based	Image processing + autocorrelation	—
Re. [15]	Data driven	Gray-level co-occurrence matrix (GLCM) + SVDD	93%
Re. [18]	Data driven	Local binary pattern (LBP) + SVM	93.3%
Proposed method	Data driven	IP + DCNN	**95.55%**

the data into the ML or DL algorithm model, and relies on the algorithm itself to fit the complex mapping between the input data and the label. Thus, compared with model-based and signal-based methods, data-driven methods do not need complex prior knowledge, and the intelligence level is higher, so more and more attention has been paid to this method in the field of damage detection. On the basis of the advantages of the data-driven method, this paper introduces the DL method for the first time in the WR visual detection field. Compared with other data-driven methods:

a) This DL-based method does not need artificial feature extraction, and relies on the CNN itself to extract the features of the original data adaptively; thus, further improving the level of intelligence, and meanwhile, reaching an advanced level of detection performance;
b) Moreover, this paper proposes a new method of WR image processing, which solves the problems of non-standard WR data that were not solved in the existing studies;
c) In addition, in the process of dataset building, we considered factors such as oil pollution, WR size, and so on, which makes the algorithm model more robust and adaptable.

Therefore, compared with the existing visual methods, this method is advanced and makes a certain contribution to the field.

2) Comparison and discussion with other nondestructive detection methods. Other non-destructive detection methods for WRs, such as the electromagnetic method, the acoustic emission method, and the ray method, are currently under further research. The electromagnetic method has been developed for the longest time and is close to the practical application, and there are some functional instruments available. The visual method is full of prospects in practical application due to the development of optical devices and algorithms; while other methods are still in the theoretical and laboratory stages. Each method has its own merits and drawbacks [6], and no method has been fully trusted by people at present in practical applications, so it is difficult to compare the relevant indicators in detail (one can refer to [18] for some discussion on our preliminary work). However, compared with other methods, the visual method is the most intuitive method to grasp the early damage of WR surface, which is objective and accurate. Furthermore, the visual method can be combined with other methods to comprehensively detect the internal and external damage of WRs. Therefore, this work is expected to play a certain role in promoting non-destructive testing methods for WRs, especially the visual method.

Overall, the proposed WR-IPDCNN can accurately and quickly identify the WR surface damage states from the images that are preprocessed by posture adjustment and ROI extraction. And it has advanced level and plays a certain promoting role in this field.

VI. Conclusions

This paper proposes an automatic detection method for WR early surface damage based on image preprocessing and a convolution neural network, aiming at the issues of WR surface damage detection, namely, unstandardized data, low detection automation/intelligence, and unsatisfactory diagnostic results. The main conclusions are as follows: A kind of vision perception system is designed, which can collect the surface image of steel WRs in the circumferential direction; a new image preprocessing method for WR is proposed to normalize the circumferential irregular image data of WR surfaces; the WR-PA method can adjust the posture of the WRs, and the WR-ROI can realize the foreground extraction and segmentation of the WR images; an improved CNN named WR-IPDCNN is proposed, which uses a deeper structure to extract data features adaptively. Compared with other methods, WR-IPDCNN achieved a higher accuracy in the established dataset in this paper, achieving a 95.55% diagnostic accuracy.

In future work, we hope to realize wear degree classification and damage location. In addition, we will collect more surface images, including more WR state types, so as to promote the practical application of this method.

References

[1] H. Henao, S. M. J. R. Fatemi, G. A. Capolino, and S. Sieg-Zieba, "Wire rope fault detection in a hoisting winch system by motor torque and current signature analysis," *IEEE Transactions on Industrial Electronics*, vol. 58, pp. 1727–1736, 2011.

[2] S. M. Pan, D. L. Zhang, and E. C. Zhang, "Nondestructive testing for shallow defect of ferromagnetic objects based on magnetic probe structure," *IEEE Transactions on Magnetics*, vol. 54, no. 11, Nov. 2018.

[3] J. Krešák, P. Peterka, S. Kropuch, and L. Novákb, "Measurement of tight in steel ropes by a mean of thermovision," *Measurement*, vol. 50, pp. 93–98, Apr. 2014.

[4] H. Mouradi, A. El Barkany, and A. El Biyaali, "Steel wire ropes failure analysis: experimental study," *Engineering Failure Analysis*, vol. 91, pp. 234–242, Sep. 2018.

[5] Y. X. Peng, X. D. Chang, S. S. Sun, Z. C. Zhu, X. S. Gong, S. Y. Zou, W. X. Xu, and Z. T. Mi, "The friction and wear properties of steel wire rope sliding against itself under impact load," *Wear*, vol. 400–401, pp. 194–206, Apr. 2018.

[6] S. Z. Yang, Y. H. Kang, H. G. Chen, J.M. Yuan, "Electromagnetic nondestructive testing of wire ropes," *Beijing, China: Machinery Industry Press*, pp. 5–22, 2017.

[7] J. Zhang, X. Tan, and P. Zheng, "Non-destructive detection of wire rope discontinuities from residual magnetic field images using the hilbert-huang transform and compressed sensing," *Sensors*, vol. 17, no.3, 608, Mar. 2017.

[8] C. Piciarelli, D. Avola, D. Pannone, and G. L. Foresti, "A vision-based system for internal pipeline inspection," *IEEE Transactions on Industrial Informatics*, vol. 15, no. 6, Jun. 2019.

[9] J. Gan, Q. Li, J. Wang, and H. Yu, "A hierarchical extractor-based visual rail surface inspection system," *IEEE Sensors Journal*, vol. 17, no. 23, pp. 7935–7944, Dec. 2017.

[10] S. H. Hanzaei, A. Afshar, and F. Barazandeh, "Automatic detection and classification of the ceramic tiles' surface defects," *Pattern Recognition*, vol. 66, pp. 174–189, Jun. 2017.

[11] B. Li, G. Thomas, and D. Williams, "Detection of ice on power cables based on image texture features," *IEEE Transactions on Instrumentation and Measurement*, vol. 67, no. 3, pp. 497–504, Mar. 2018.

[12] A. Vallan and F. Molinari, "A vision-based technique for lay length measurement of metallic wire ropes," *IEEE Transactions on Instrumentation and Measurement*, vol. 58, no. 5, pp. 1756–1762, May. 2009.

[13] E. S. Platzer, H. Süße, J. Nägele, K. H. Wehking, and J. Denzler, "On the Suitability of different features for anomaly detection in wire ropes," *Communications in Computer and Information Science*, vol. 68, pp. 296–308, Springer, Berlin, Heidelberg, 2009.

[14] E. S. Platzer, J. Nägele, K. H. Wehking, and J. Denzler, "HMM-based defect localization in wire ropes–a new approach to unusual subsequence recognition," *In Proceedings of the Dagm Symposium*, Jena, Germany,

pp. 442–451, Sep. 2009.

[15] H. X. Sun, Y. H. Zhang and F. L. Luo, "Texture defect detection of wire rope surface with support vector data description," *In 2009 Chinese Conference on Pattern Recognition*, pp. 721–725, Nov 2009.

[16] E. S. Wacker and J. Denzler, "Enhanced anomaly detection in wire ropes by combining structure and appearance," *Pattern Recognition Letters*, vol. 34, pp. 942–953, Jun. 2013.

[17] O. Yaman and M. Karakose, "Auto-correlation based elevator rope monitoring and fault detection approach with image processing," *In Proceedings of the 2017 International Artificial Intelligence and Data Processing Symposium (IDAP)*, Malatya, Turkey, 16–17 Sep. 2017.

[18] P. Zhou, G. B. Zhou, Z. Z. He, C. Q. Tang, Z. Z. Zhu, and W. Li, "A novel texture-based damage detection method for wire ropes," *Measurement*, vol. 148, 106954, Dec. 2019.

[19] Y. LeCun, Y. Bengio, and G. Hinton, "Deep learning," *Nature*, vol. 521, pp. 436–444, May. 2015.

[20] W. J. Sun, R. Zhao, R. Q. Yan, S. Shao, and X. F. Chen, "Convolutional discriminative feature learning for induction motor fault diagnosis," *IEEE Transactions on Industrial Informatics*, vol. 13, no. 3, pp. 1350–1359, Feb. 2017.

[21] J. S. L. Senanayaka, V. K. Huynh, and K. G. Robbersmyr, "Multiple classifiers and data fusion for robust diagnosis of gearbox mixed faults," *IEEE Transactions on Industrial Informatics*, vol. 15, no. 8, pp. 4569–4579, Aug. 2019.

[22] S. S. Udmale, S. S. Patil, V. M. Phalle, and S. K. Singh, "A bearing vibration data analysis based on spectral kurtosis and ConvNet," *Soft Computing*, vol. 23, no. 19, pp. 9341–9359, Oct. 2019.

[23] O. Janssens, V. Slavkovikj, B. Vervisch, K. Stockman, M. Loccufier, S. Verstockt, R. V. D. Walle, S. V. Hoecke, "Convolutional neural network based fault detection for rotating machinery," *Journal of Sound and Vibration*, vol. 337, pp.331–.345, Sep. 2016.

[24] L. Wen, X. Li, L. Gao, and Y. Y. Zhang, "A new convolutional neural network-based data-driven fault diagnosis method," *IEEE Transactions on Industrial Electronics*, vol. 65, no. 7, pp. 5990–5998, Jul. 2018.

[25] G. Q. Jiang, H. B. He, J. Yan, and P. Xie, "Multiscale convolutional neural networks for fault diagnosis of wind turbine gearbox," *IEEE Transactions on Industrial Electronics*, Vol. 66, no. 4, pp. 3196–3207,Apr. 2019.

[26] Y. G. Lei, B. Yang, X. W. Jiang, F. Jia, N. P. Li, and A. K. Nandi, "Applications of machine learning to machine fault diagnosis: A review and roadmap," *Mechanical Systems and Signal Processing*, vol. 138, 106587, Apr. 2020.

[27] R. Zhao, R. Q. Yan, Z. H. Chen, K. Z. Mao, P. Wang, and R. X. Gao, "Deep learning and its applications to machine health monitoring," *Mechanical Systems and Signal Processing*, vol. 115, pp. 213–237, Jan. 2019.

[28] L. M. Xiao, C. Li, Z. Z. Wu, and T. Wang, "An enhancement method for x-ray image via fuzzy noise removal and homomorphic filtering," *Neurocomputing*, vol. 195, pp. 56–64, Jun. 2016.

[29] C. L. Yang, P. Y. Liu, G. F. Yin, H. H. Jiang, and X. Q. Li, "Defect detection in magnetic tile images based on stationary wavelet transform," *NDT & E International*, vol. 83, pp.78–87, Oct. 2016.

[30] J. E. Arco, J. M. Górriz, J. Ramírez, I. Álvarez, and C. G. Puntonet, "Digital image analysis for automatic enumeration of malaria parasites using morphological operations," *Expert Systems with Applications*, vol. 42, no. 6, pp. 3041–3047.

[31] K. P. White, B. Kundu, and C. M. Mastrangelo, "Classification of defect clusters on semiconductor wafers via the Hough transformation," *IEEE Transactions on Semiconductor Manufacturing*, vol. 21, no. 2, pp. 272–278, May. 2008.

[32] H. Zhang, X. T. Jin, Q. M. J. Wu, Y. N. Wang, Z. D. He, and Y. M. Yang, "Automatic visual detection system of railway surface defects with curvature filter and improved gaussian mixture model," *IEEE Transactions on Instrumentation and Measurement*, vol. 67, no. 7, pp. 1593–1608, Jul. 2018.

[33] G. B. Kshirsagar and N. D. Londhe, "Improving performance of devanagari script input-based p300 speller using deep learning," *IEEE Transactions on Biomedical Engineering*, vol. 66, no. 11, pp. 2992–3005, Nov. 2019.

[34] A. Ibrahim, A. Dalbah, A. Abualsaud, U. Tariq, and A. El-Hag, "Application of machine learning to evaluate insulator surface erosion," *IEEE Transactions on Instrumentation and Measurement*, vol. 69, no. 2, pp. 314–316, Feb. 2020.

[35] L. Song, X. Li, Y. Yang and X. J. Zhu. "Detection of micro-defects on metal screw surfaces based on deep convolutional neural networks," *Sensors*, vol. 18, no. 11, Oct. 2018.

[36] F. Chen and M. R. Jahanshahi, "NB-CNN: deep learning-based crack detection using convolutional neural network and Naïve Bayes data fusion," *IEEE Transactions on Industrial Electronics*, vol. 65, no. 5, pp. 4392-4400, May. 2018.

[37] A. Khumaidi, E. M. Yuniarno and M. H. Purnomo, "Welding defect classification based on convolution neural network (CNN) and Gaussian kernel," *2017 International Seminar on Intelligent Technology and Its Applications (ISITIA), IEEE*, Surabaya, pp. 261-265, Aug. 2017.

[38] H. Q. Jiang, S. He and J. M. Gao. "An improved convolutional neural network for weld defect recognition," *Journal of Mechanical Engineering*, vol. 56, no.8, Apr. 2020.

[39] Y. P. Gao, L. Gao and X. Y. Li. "A semi-supervised convolutional neural network-based method for steel surface defect recognition," *Robotics and Computer Integrated Manufacturing*, vol.61, 101825, Feb. 2020.

[40] S. Cheon, H. Lee, C. O. Kim and S. H. Lee, "Convolutional neural network for wafer surface defect classification and the detection of unknown defect class," *IEEE Transactions on Semiconductor Manufacturing*, vol. 32, no. 2, pp. 163-170, May 2019.

[41] J. Chen, Z. Liu, H. Wang, A. Núñez and Z. Han, "Automatic defect detection of fasteners on the catenary support device using deep convolutional neural network," *IEEE Transactions on Instrumentation and Measurement*, vol. 67, no. 2, pp. 257-269, Feb. 2018.

[42] Q. Luo, X. Fang, L. Liu, C. Yang and Y. Sun, "Automated visual defect detection for flat steel surface: a survey," *IEEE Transactions on Instrumentation and Measurement*, vol. 69, no. 3, pp. 626-644, Mar. 2020.